

## Multimodal azimuthal oscillations in electron beam generated $E \times B$ plasma

Nirbhav Singh Chopra<sup>1,2</sup>, Mina Papahn Zadeh<sup>3</sup>, Mikhail Tyushev<sup>3</sup>, Andrei Smolyakov<sup>3</sup>, Alexandre Likhanskii<sup>4</sup>, and Yevgeny Raitses<sup>1</sup>

<sup>1</sup> Princeton Plasma Physics Laboratory, Princeton University, Princeton, NJ 08543, United States of America

<sup>2</sup> Department of Astrophysical Sciences, Princeton University, Princeton, NJ 08544, United States of America

<sup>3</sup> Department of Physics and Engineering Physics, University of Saskatchewan, Saskatoon SK S7N 5E2, Canada

<sup>4</sup> Applied Materials Inc, 35 Dory Rd, Gloucester, MA 01930, United States of America

### Abstract

Electron beam (e-beam) generated plasmas with applied crossed electric and magnetic ( $E \times B$ ) fields are promising for low-damage material processing. However, these plasmas can be subject to the formation of azimuthally propagating structures that enhance the radial transport of energetic charged species, which can harm the gentle processing capability of the plasma. In this work we investigate the azimuthal structure formation in an e-beam generated  $E \times B$  plasma using experimental diagnostics and 2D3V particle-in-cell simulations. Our findings demonstrate the formation of multiple simultaneously occurring azimuthally propagating modes that exhibit nontrivial radial dependence. It is suggested that the multimodal azimuthal spectrum is caused in part by the radial outflow of ions in the plasma.

### 1. Introduction

Electron beam (e-beam) generated plasmas with applied electric and magnetic ( $E \times B$ ) fields are promising for applications requiring efficient generation of ions and radicals in low pressure environments.<sup>1–7</sup> A key capability of magnetically confined e-beam plasma sources is that they can generate reactive species while maintaining low energetic particle flux to substrates placed in the periphery of the plasma region.<sup>8–11</sup>

In many axisymmetric  $E \times B$  plasma systems, such as Penning discharges, Hall discharges, sputtering magnetrons, and Bernas sources, electrons are magnetized (electron Hall parameter  $\Omega_e = \omega_{ce}/\nu_e \gg 1$ , where  $\omega_{ce}$  and  $\nu_e$  are the electron cyclotron and electron collision frequencies), while ions are usually non-magnetized (ion Hall parameter  $\Omega_i = \omega_{ci}/\nu_i \ll 1$ , where  $\omega_{ci}$  and  $\nu_i$  ion cyclotron and ion collision frequencies) or very weakly magnetized ( $\Omega_i \lesssim 1$ ).<sup>12–16</sup> Therefore, ion transport is dominated by an ambipolar electric field and collisions with neutrals. Previous work on e-beam generated  $E \times B$  Penning plasma has demonstrated the formation of an ion-confining radial electric potential well.<sup>1,12,13</sup> This potential can be leveraged

for low-damage threshold material processing applications by limiting energetic ion flux, thereby preventing energetic ions from damaging material surfaces.

However, several operating regimes of axisymmetric  $E \times B$  plasma devices are accompanied by large-scale azimuthally propagating fluctuations in plasma density and potential ('spokes') induced by a modified Simon-Hoh instability (MSHI).<sup>12,13,16-22</sup> The spoke has been shown to energize ions in the radial direction, thereby reintroducing energetic ions to the peripheral substrate processing region.<sup>23</sup> Therefore, mitigating the formation of the spoke may enable a wider operating regime of gentle processing capability of the e-beam generated  $E \times B$  plasma.

In this work, we experimentally and computationally investigate the structure and formation of azimuthally propagating plasma structures in an e-beam generated  $E \times B$  plasma. Our experimental findings indicate the existence of two regions with distinct azimuthal mode formation. We also performed 2D3V Particle-in-cell (PIC) simulations in the plane perpendicular to the applied magnetic field to independently determine the radial macroscopic profiles and azimuthal mode spectrum. Good agreement is shown between experimental findings and the simulation.

The paper is organized as follows: Section II discusses the experimental setup of the e-beam generated  $E \times B$  plasma. Section III discussed the plasma diagnostics and measurement procedures used, as well as the PIC simulation setup. Section IV details the results of the probe measurements and their analysis, as well as the experimental validation of the PIC simulations. Analytical models of the radial electron and ion transport and azimuthal instability onset are proposed and compared to the experimental measurements in Section V. Conclusions are summarized in Section VI.

## II. Experimental setup

The experimental setup consisted of an e-beam generated  $E \times B$  plasma chamber with a conducting anticathode installed on the axially opposite side of the chamber from the cathode. The setup used in this work is nearly identical to the setup described in Ref. <sup>24</sup> and is briefly described here. The e-beam chamber is a cylindrical vacuum vessel that is pumped by a turbomolecular pump backed by a rough pump to a base pressure of  $\sim 1 \mu\text{Torr}$ . The chamber is filled with Ar gas to a pressure of 0.1 mTorr. An axial magnetic field of 75-125 G is generated by electromagnets arranged in a Helmholtz-like configuration along the chamber. The anticathode has a radius of 4.5 cm.

However, in the present setup the thermionic cathode was significantly modified, which is depicted in Figure 1. The filament is made from a 0.4 mm diameter tungsten wire, which is ohmically heated using a heater power supply with bias voltage  $V_{\text{heater}}$ . The filament length is 10 mm. The filament assembly is inserted through a stainless-steel cathode plate with radius  $R_{\text{c,plate}} = 4.5 \text{ cm}$  and is electrically isolated from the cathode plate with ceramic tubes so that heater current does not pass directly through the cathode plate body. Both the thermionic filament and the cathode plate are biased to the applied cathode bias voltage  $V_c = -55 \text{ V}$ . The

discharge current is measured using a current shunt on the cathode and is  $I_d = 100$  mA. The modified cathode increases the region of axial electron confinement to the radial extent of the cathode plate  $R_{c,plate}$ .<sup>24</sup>

In this work, the anticathode is biased to the cathode potential so that is electron repelling, i.e. operated in 'repeller mode' with anticathode bias potential  $V_{atc} = V_c$ . This is in contrast to 'collector mode', whereby the anticathode is biased to the anode potential  $V_{atc} = 0$  V and therefore collects nearly all incident electrons. The effect of the anticathode operating in collector mode is not considered in the present work.

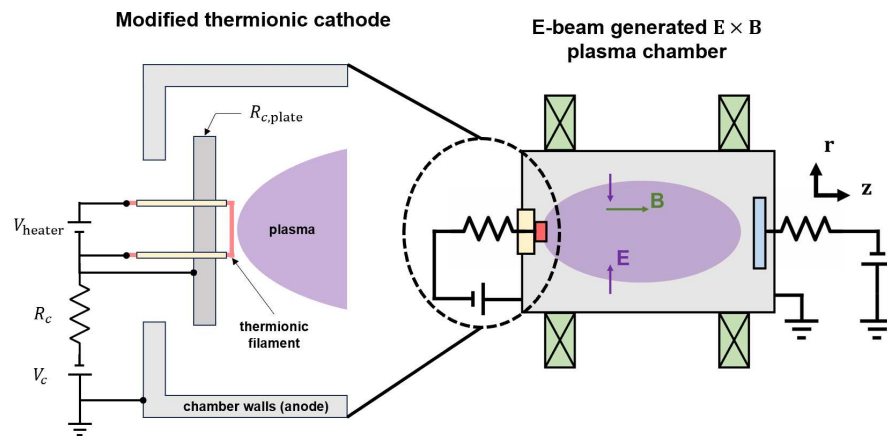


**Figure 1.** Schematic of modified thermionic cathode installed on e-beam generated  $E \times B$  chamber.

### III. Methods

#### 1. Diagnostics and measurement procedure

A Langmuir probe (LP) and emissive probe (EP) diagnostic were mounted at the axial midplane of the chamber and were used to determine the electron energy distribution function (EEDF), electron density, electron temperature, and plasma potential at different radii. These diagnostics are described in further detail in Ref. <sup>24</sup>.

The coherent azimuthal plasma density oscillations were determined by an azimuthally oriented ion probe array that was mounted at the axial midplane of the chamber (Figure 2). The ion probe array consists of two negatively biased tungsten wires with identical exposed collecting areas, each with diameter 1.1 mm and exposed wire length of 1.7 mm. Each tungsten

wire is inserted into a ceramic tube of outer diameter 2.1 mm. The probe tips are separated by a distance  $\Delta x = 2.1$  cm such that the azimuthal angle subtended by the probe array is given by  $\theta_{12} = 2 \arctan(\Delta x/2r_0)$ , where  $r_0$  is the probe array retraction depth. As a result, the radial distance of the probe tips to the geometric center of the plasma is given by  $r = \sqrt{(\frac{\Delta x}{2})^2 + r_0^2}$ . The geometric properties of the probe array shown in Table I.

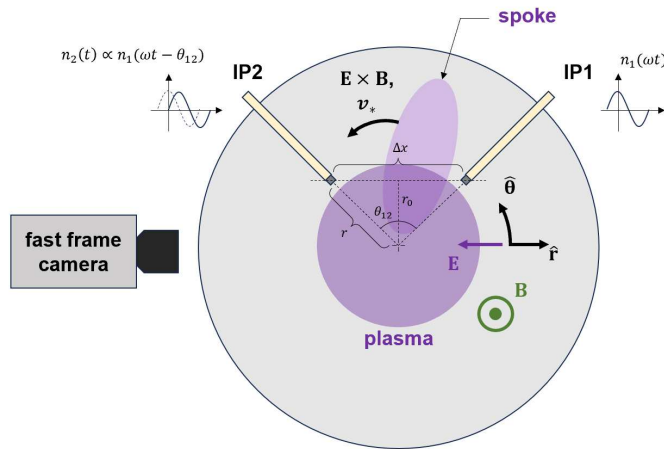


**Figure 2.** Schematic of diagnostic setup for azimuthal oscillation characterization. The e-beam is injected in the  $+\hat{z}$  direction. Also shown is the direction of  $\mathbf{E} \times \mathbf{B}$  and electron diamagnetic drift velocity  $\mathbf{v}_*$ .

**Table I.** Geometric properties of the probe array.

$r_0$ [cm]	$r$ [cm]	$\theta_{12}$ [rad] ([deg])
1.0	1.5	1.6 (93°)
2.0	2.3	1.0 (55°)
3.0	3.2	0.7 (39°)

The tungsten wire is individually biased to a potential of  $V_b = -100$  V relative to the grounded chamber walls, such that the probe ion collection is in an orbital motion limited (OML) regime. Under such conditions, the ion current  $I_j$  collected by the  $j$ th ion probe ( $j = 1$  or  $2$  corresponding to ion probe 1 (IP1), and ion probe 2 (IP2)) is independent of the electron temperature and is proportional to the local plasma density,<sup>25,26</sup>

$$I_j(t) = \frac{2}{\sqrt{\pi}} en_j(t) A_{pr} \sqrt{-\frac{e(V_b - V_{pl})}{2\pi m_i}}, \quad (1)$$

where  $n_j(t)$  is the temporally fluctuating plasma density at the  $j$ th probe,  $A_{pr}$  is the probe collection area,  $V_{pl}$  is the plasma potential, and  $m_i$  is the Argon ion mass. Here the plasma is assumed to be quasineutral,  $n_j \approx n_i \approx n_e$  where  $n_i$  and  $n_e$  are the ion and electron densities respectively.

A two point-correlation technique is used to determine the azimuthally coherent portion of the fluctuating signal collected by each ion probe. The cross power spectral density (CSD) is used to quantitatively determine the coherence and relative phase of  $n_1(t)$  and  $n_2(t)$ .<sup>27,28</sup> Representative ion current signals collected by IP1 and IP2 and their cross spectral density  $P_{12}$  are shown in Figure 3. The CSD is defined as the Fourier transform of the cross-correlation of the two signals,<sup>28</sup>

$$P_{12}(f) \equiv \int_{-\infty}^{\infty} \left[ \int_{-\infty}^{\infty} n_1(t) n_2(t + \tau) dt \right] e^{-i2\pi f \tau} d\tau \quad (2)$$

$$\equiv F \left( \int_{-\infty}^{\infty} n_1(t) n_2(t + \tau) dt \right).$$

where  $f$  is the frequency. The cross-coherence is defined as<sup>28</sup>

$$C_{12}(f) \equiv \frac{|P_{12}|^2}{|P_{11}| |P_{22}|}, \quad (3)$$

which quantifies the fraction of spectral power transferred from  $n_1$  to  $n_2$ , for each spectral component  $f$ . Moreover, the argument of the CSD,  $\text{Arg}(P_{12})$ , quantifies the relative phase between  $n_1$  and  $n_2$  for each spectral component  $f$ . Here the argument function is taken to have the convention that for a complex valued function  $g$ ,  $\pi < \text{Arg}(g) \leq \pi$ .

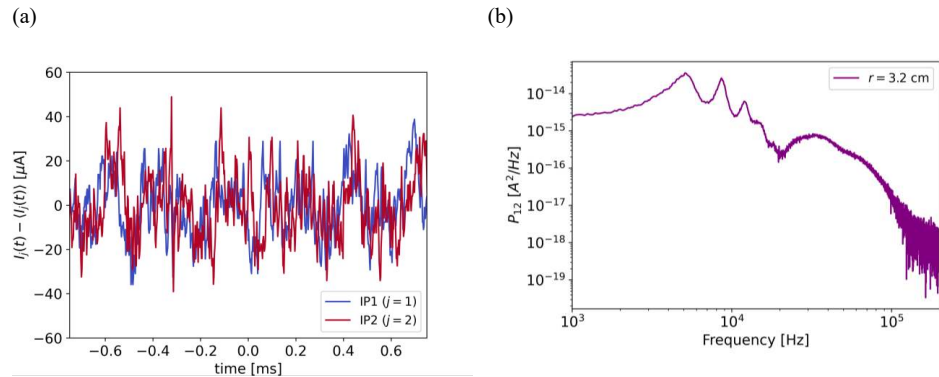


**Figure 3.** (a) Ion current temporal signal  $I_j(t)$  determined by IP1 ( $j = 1$ ) and IP2 ( $j = 2$ ) for  $B = 100$  G,  $V_c = -55$  V,  $p = 0.1$  mTorr, with mean signal subtracted (b) Cross spectral density  $P_{12}$  of  $I_1$  and  $I_2$ .

Azimuthal oscillations were also independently determined by a fast frame camera. A Phantom v7.3 high speed camera operating at 95 kfps imaged the optical emission of the plasma in the  $r - z$  plane (Figure 2). The fast frame images were then averaged along the axial ( $z$ ) direction and Fourier transformed in time to determine the radial dependence of the plasma emission oscillations.

## 2. Particle in-cell method

A 2D3V particle-in-cell method (PIC) was developed using the WarpX code<sup>29</sup> to simulate the electron beam generated  $E \times B$  plasma in the plane perpendicular to the applied magnetic field and are similar to the simulations described in Ref. <sup>30</sup>. The code is run on the Digital Research Alliance of Canada Mist server with one NVIDIA V100-SMX2-32GB GPU per simulation. The simulation domain is indicated in Figure 4, and relevant simulation parameters are shown in Table II. Simulations were performed to most closely emulate the conditions of the experimental setup. One step electron-Argon impact ionization ( $Ar + e \rightarrow Ar + e + e$ , Ref. <sup>31</sup>), electron-Argon excitation ( $Ar + e \rightarrow Ar^* + e$ , Ref. <sup>32</sup>), and electron-Argon elastic (Ref. <sup>33</sup>) scattering reactions were included. The simulation is initialized with an electron beam population that is injected into a background of neutral Argon. After an initial transient period, a self-consistent quasi steady-state discharge is sustained through the above-mentioned electron collisional processes and electron and ion losses to the absorbing boundary of the domain.

The major difference between the PIC setup and the experimental setup is the geometry of the anode in the computational domain, which is a square with side lengths  $L_x = L_y = 10$  cm. This is compared to the experimental chamber, which is a cylindrical vacuum vessel with a diameter of  $D_{\text{expt.}} = 20$  cm. Azimuthal oscillations and time averaged radial profiles of electron density, temperature, and plasma potential are determined from the PIC simulations and are compared to the experimental measurements. The temporal spectra of the azimuthal oscillations occurring in the PIC simulations were determined by the multiple signal classification (MUSIC) super-resolution signal processing method.<sup>23,34</sup>

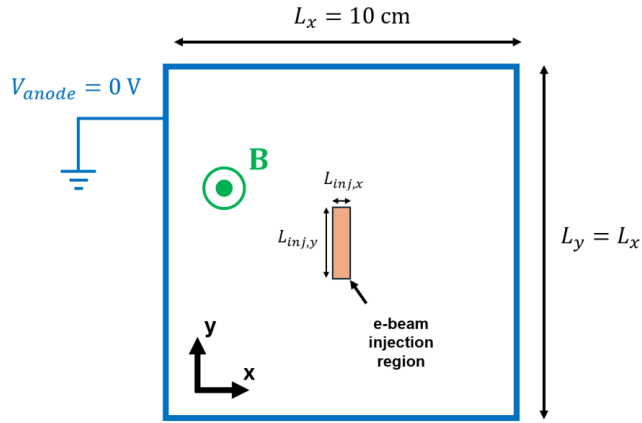


**Figure 4.** Diagram of simulation domain.

**Table II.** Parameters of the PIC simulations used in this work. Symbols used in this table:  $\lambda_{pe}$  – minimum electron Debye length;  $C$  – maximum Courant number;  $N_{\text{macro.}}$  – number of physical particles per macroparticle;  $L_{inj,x,y}$  – side length of rectangular electron beam injection region in  $x,y$  direction;  $I_{inj}$  – injected electron beam current;  $\epsilon_b$  – injected electron beam energy.

Parameter	Value
$\Delta x$	0.130 mm
$\Delta t$	$1.7 \times 10^{-11}$ s
$\lambda_{pe}$	0.150 mm
$C$	0.26
$N_{\text{macro.}}$	$1.0625 \times 10^7$
$L_x = L_y$	10 cm
$L_{inj,x}$	0.4 mm
$L_{inj,y}$	10 mm
$I_{inj}$	100 mA
$p$	0.1 mTorr (Argon)
$B$	100 G
$\epsilon_b$	55 eV

## IV. Results

### 1. Experimental measurements

The Fourier spectra of the plasma density fluctuation  $F(n_1(t))$  at  $r = 1.5$  cm and 3.2 cm are shown in Figure 5, for operating conditions  $V_c = -55$  V,  $B = 100$  G,  $p = 0.1$  mTorr. Both  $r = 1.5$  cm and  $r = 3.2$  cm measurements show prominent low frequency modes occurring at  $f_0 = 5 - 7$  kHz and the double frequency harmonic  $f_1 \approx 2f_0$ , with  $f_1$  increasing in amplitude at

$r = 3.2$  cm. There is also a higher frequency mode  $f_H = 30$  kHz that is more prominent at  $r = 1.5$  cm.

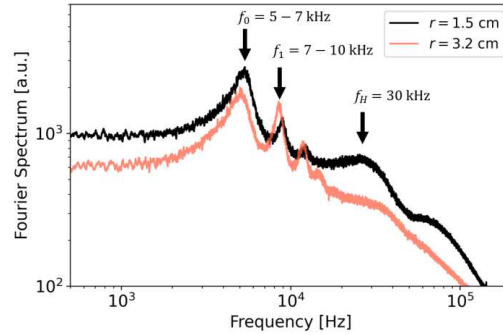


**Figure 5.** FFT of ion density temporal trace determined by IP1, measured at  $r = 1.5$  cm and  $r = 3.2$  cm. Parameters are  $B = 100$  G,  $V_c = -55$  V,  $p = 0.1$  mTorr.

The cross coherence of  $n_1(t)$  and  $n_2(t)$ ,  $C_{12}(f)$  is shown in Figure 6, for the same experimental parameters. Figure 6 a and b indicate that at  $r = 1.5$  cm both low and high frequency modes at  $f_0$  and  $f_H$  have a high coherence with  $C_{12} > 0.5$ . Moreover, both modes obey  $\text{Arg}(P_{12}(f_0)) \approx \text{Arg}(P_{12}(f_H)) \approx -\theta_{12}$ , indicating both  $f_0$  and  $f_H$  are single lobed ( $m = 1$ ) modes that are azimuthally propagating in the  $+E \times B$  direction. At  $r = 3.2$  cm, the coherence of the low frequency mode remains high  $C_{12}(f_0) > 0.8$ , while the high frequency mode coherence reduces  $C_{12}(f_H) < 0.5$ . The azimuthally propagating modes occurring at  $f_0$  and  $f_H$  are also corroborated by the fast frame imaging diagnostic (Appendix 1).



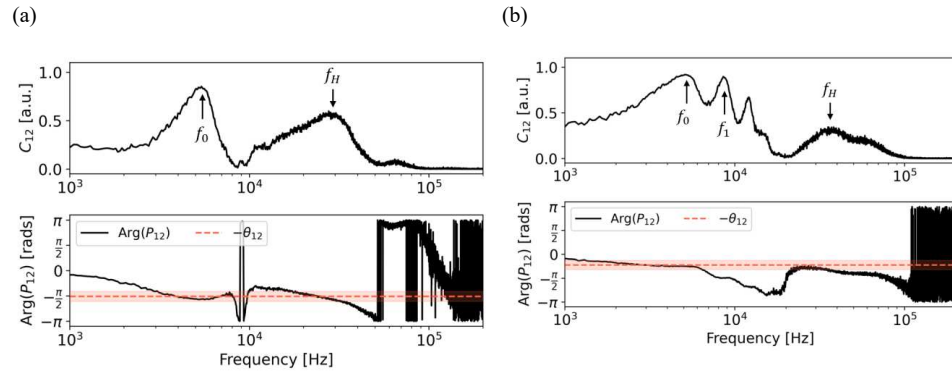


**Figure 6.** Cross coherence and argument of cross spectral density of ion density temporal traces, measured at (a)  $r = 1.5$  cm, (b)  $r = 3.2$  cm. Parameters  $B = 100$  G,  $p = 0.1$  mTorr,  $V_c = -55$  V. The modes  $f_0$ ,  $f_1$ , and  $f_H$  are also labelled.

The cross-coherence dependence on the applied magnetic field is shown for  $r = 1.5$  cm and  $r = 3.2$  cm in Figure 7. A trend of enhancement in the coherence of  $f_0$  and  $f_1$  and suppression of  $f_H$  can be observed for increasing magnetic field. This trend is also confirmed by the fast frame image analysis (Appendix 1).

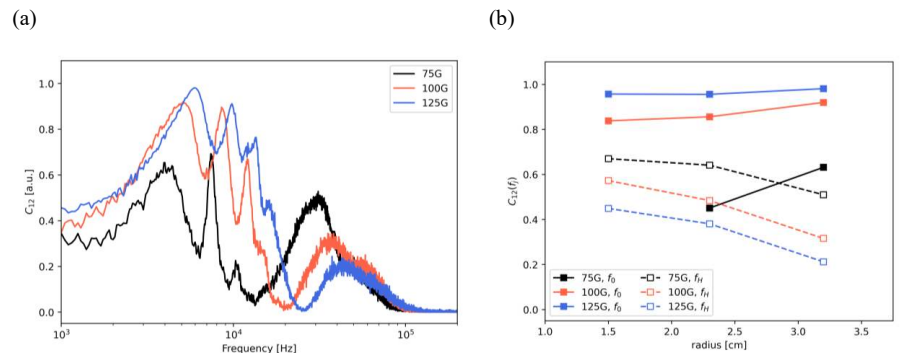


**Figure 7.** (a) Ion probe cross coherence spectra measured at  $r = 3.2$  cm for several values of the applied magnetic field (b) Mode cross coherence vs. radial coordinate for the low frequency mode  $f_0$  and high frequency mode  $f_H$  for several magnetic fields. Experimental parameters are  $p = 0.1$  mTorr,  $V_c = -55$  V.

## 2. Experimental validation of 2D PIC model

A snapshot of the ion density computed by the PIC simulation after reaching quasi-steady state is shown in Figure 8. Also shown are the azimuthal and radial components of the wavevector associated with the observed density wave,  $\mathbf{k} = k_r \hat{\mathbf{r}} + k_\theta \hat{\boldsymbol{\theta}}$ . Indeed an azimuthally

rotating plasma density structure is observed propagating in the  $+E \times B$  direction. Furthermore, the simulation indicates that the rotating spoke is accompanied by both radially outward and inward propagating wavevectors components: ahead of the spoke,  $k_r < 0$ , while behind the spoke,  $k_r > 0$ .

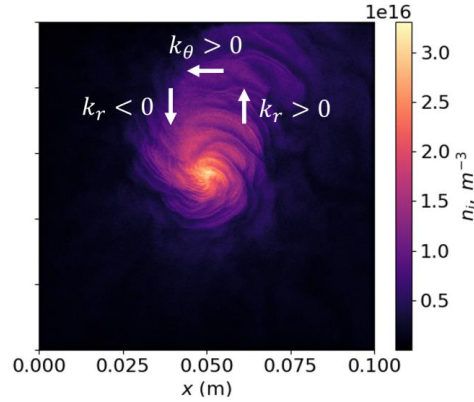


**Figure 8.** Snapshot of ion density after simulation reaches saturation. Also indicated are characteristic azimuthal and radial components of the wavevector.

A comparison of radial profiles of electron density, electron temperature, plasma potential, and azimuthal pseudospectra determined experimentally and from the PIC simulations are shown in Figure 9. The normalized radial coordinate is defined as  $\rho = r/(D_{\text{expt.}}/2)$  for the experimental setup and  $\rho = r/(L_x/2)$  for the simulation setup. The time averaged electron density, electron temperature, and plasma potential radial profiles all show good agreement.

The MUSIC spectra determined by the PIC simulation reproduces the occurrence of multiple coherent azimuthal modes. However, the frequency of the azimuthal modes in the simulation are larger than in experiment by approximately a factor of 2. This may be due to the radius of the computational domain being smaller than the experimental chamber radius by a factor of 2. Indeed, previous works have demonstrated increasing computational domain size reduces the frequency of azimuthal oscillations in e-beam generated  $E \times B$  plasmas.<sup>23</sup>

Quantitative agreement in the mode peak frequencies is observed between the simulated MUSIC spectrum and the experimentally determined cross-coherence when the frequency transformation  $f_{\text{expt.}} = f_{\text{sim.}} \cdot (D_{\text{expt.}}/L_x) = 2f_{\text{sim.}}$  is applied to the experimental cross-coherence. This speculation should be further investigated by performing PIC simulations with a computational domain radius equal to the experimental chamber radius.

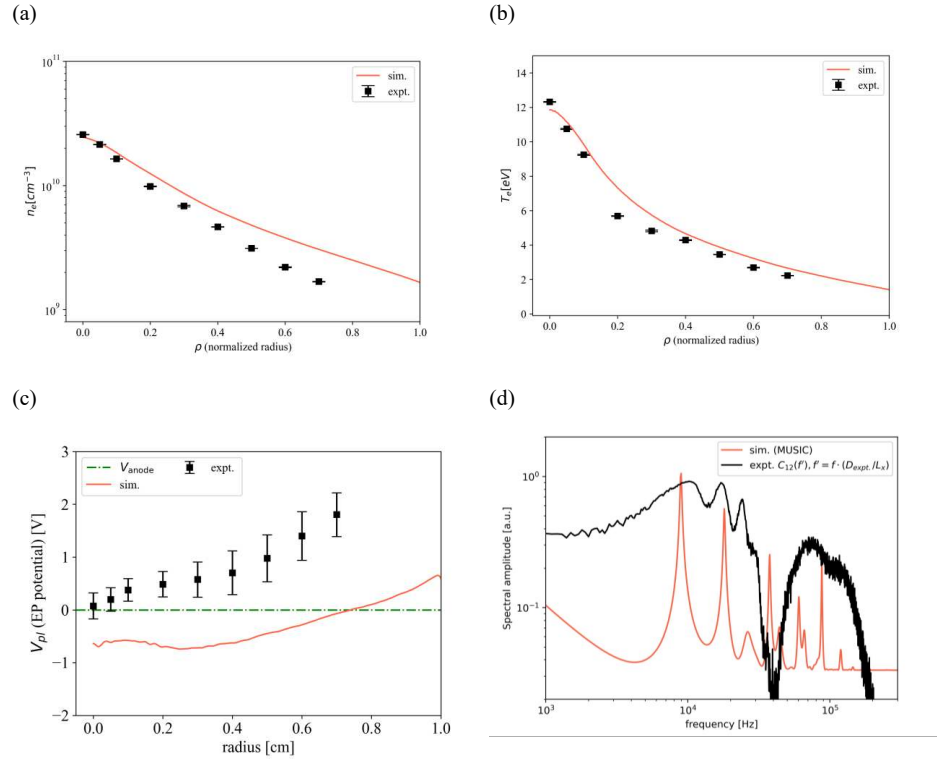


**Figure 9.** Validation of radial profiles determined by experiment (expt.) and simulation (sim.) for (a) Electron density  $n_e$ , (b) Electron temperature  $T_e$ , and (c) Plasma potential  $V_{pl}$ . Parameters are  $B = 100$  G,  $p = 0.1$  mTorr,  $V_c = -55$  V. (d) Density fluctuation azimuthal pseudospectra for  $\rho = 0.32$  (expt.: cross-coherence  $C_{12}$ , sim.: MUSIC spectrum). The experimental cross-coherence spectrum frequency has been increased by the scaling ratio  $D_{expt}/L_x = 2$ .

## V. Discussions

### 1. Radial electron and ion transport

Here we apply a 1-dimensional model to determine the cross field anomalous electron transport in the radial direction, which is based on the electron continuity equation. This model is closely related to the 0-dimensional model developed in Ref. <sup>24</sup>. Additionally, we apply a 1-dimensional model of the ion continuity equation to determine the radial outflow velocity of ions, which is used further in Section V.2 to determine the onset of the modified Simon-Hoh instability. The electron and ion continuity equations are given by

$$\nabla \cdot \mathbf{\Gamma}_e = R_{iz}, \quad (4)$$

$$\nabla \cdot \mathbf{\Gamma}_i = R_{iz}, \quad (5)$$

where  $\mathbf{\Gamma}_e$  and  $\mathbf{\Gamma}_i$  are the local electron and ion fluxes respectively and  $R_{iz}$  is the volumetric ionization rate given by

$$R_{iz} = n_g \left( \frac{2}{m_e} \right)^{1/2} \int_0^\infty d\varepsilon \sigma_{iz}(\varepsilon) \varepsilon^{1/2} f_e(\varepsilon), \quad (6)$$

with the gas density  $n_g = p/kT_g$  and neutral gas temperature assumed to be  $T_g = 300\text{K}$ . Integrating Eqs. (4) and (5) over a cylindrical control volume of length  $L_{ch}$  and radius  $r$ , and solving for the radial flux, we find

$$\bar{\Gamma}_e^r(\alpha) = \bar{\Gamma}_e^b + \bar{R}_{iz} - \bar{\Gamma}_{e,\text{loss}}^z, \quad (7)$$

$$\bar{\Gamma}_i^r = \bar{R}_{iz} - \bar{\Gamma}_i^z, \quad (8)$$

where  $\bar{\Gamma}_{e,\text{loss}}^z$ ,  $\bar{\Gamma}_e^r(\alpha)$ ,  $\bar{\Gamma}_e^b$ ,  $\bar{\Gamma}_i^z$  and  $\bar{\Gamma}_i^r$  are the surface integrated axial electron loss flux, radial electron flux, injected electron beam flux, axial ion flux, and radial ion flux respectively, and  $\bar{R}_{iz}$  is the volume integrated ionization rate. The semi-empirically determined anomalous parameter  $\alpha$  is the inverse Hall parameter. The quantities expressed in Eqs. (7) and (8) are explicitly defined as

$$\bar{\Gamma}_{e,\text{loss}}^z = 2\pi \int_0^r r' dr' \frac{n_e v_{the}}{4} \left\{ \exp\left(-\frac{(V_{pl} - V_c)}{kT_e}\right) + \min\left[\exp\left(-\frac{(V_{pl} - V_{atc})}{kT_e}\right), 1\right] \right\}, \quad (9)$$

$$\bar{\Gamma}_e^r(\alpha) = -\mu_{e\perp}(\alpha) \left( n_e E_r + \frac{\nabla p_e}{e} \right) \cdot (2\pi L_{ch} r), \quad (10)$$

$$\bar{R}_{iz}(r) = 2\pi L_{ch} \int_0^r r' dr' R_{iz}, \quad (11)$$

$$\bar{\Gamma}_i^z = 2 \times 2\pi \int_0^r r' dr' (0.61 n_e v_{\text{Bohm}}), \quad (12)$$

and the injected electron beam flux is approximately the discharge current  $\bar{\Gamma}_e^b \approx I_d/e$ . Here we make the approximations that the net axial flux of electrons is given by the electron thermal flux confined by the cathode and anticathode sheaths. We also assume axial uniformity, that the radial electron flux is given by the drift-diffusion approximation, and that the EEDF is isotropic. Furthermore, we assume the cathode and anticathode sheaths are planar and therefore approximate the axial ion flux as the Bohm current, with the sheath density  $n_s = 0.61 n_e$  and ion velocity entering the sheath as  $v_{\text{Bohm}} = (k_B T_e / m_{Ar})^{0.5}$  where  $m_{Ar}$  is the mass of an Argon ion. The prefactor of 2 occurring in Eq. (12) accounts for Bohm ion current collected by both the anticathode and cathode surfaces. Finally, we neglect the Simon effect for electrons ‘short circuiting’ across the magnetic field lines through the axial conducting boundaries.<sup>35,36</sup> We make this assumption since the discharge is operated in repeller mode, in which case both anticathode

and cathode have a large electron reflecting sheath. Under such conditions negligible electron flux will strike either conducting boundary.

In a previous work on a similar e-beam generated  $E \times B$  plasma, it was determined that electron-neutral collisions are insufficient to explain the electron cross field transport, and electron transport rather is so-called anomalous, i.e. driven by effective electron collisions with fluctuations in the plasma.<sup>24</sup> In the case of anomalous cross field electron transport such that  $v_{en} \ll \alpha \omega_{ce}$ , the electron cross-field mobility can be approximated as  $\mu_{e\perp}(\alpha) \approx \alpha/B$ .<sup>37-39</sup> Under such conditions, Eq. (7) can be solved for the anomalous parameter,

$$\alpha(r) = \frac{\bar{\Gamma}_e^b + \bar{R}_{iz} - \bar{\Gamma}_{e,loss}^z}{-\frac{1}{B} \left( n_e E_r + \frac{\nabla p_e}{e} \right) 2\pi r L_{ch}}. \quad (13)$$

The anomalous parameter  $\alpha$  as a function of the radial coordinate is shown for several values of the applied magnetic field in Figure 10. The statistically determined anomalous parameter using the mean-squared ion density fluctuation determined from IP1,  $\alpha_{YR} = 0.25 \pi (n - n_0)^2 / n_0^2$ , as derived by Ref.<sup>37</sup>, is also shown.

Both the model based on Eq. (13) and the statistically determined  $\alpha_{YR}$  agree in the trend of relatively low value of the anomalous transport factor in the region  $r \leq 2$  cm, with sharply increasing anomaly for  $r > 2$  cm. Additionally, both  $\alpha_{mod.}$  and  $\alpha_{YR}$  tend to increase with increasing magnetic field, indicating higher cross field electron transport at larger magnetic fields. This trend predicted by the model agrees with the observation of enhanced mode coherence at larger magnetic field observed from the azimuthal ion probe measurements (Figure 7). Therefore, the enhancement of anomalous transport in the  $r > 2$  cm is likely due to the enhancement of the spoke.

The modeled anomalous parameter is reduced significantly by at least a factor of 2 at  $r = 1.5$  cm compared to  $r = 3.2$  cm. This is caused by the enhanced ionization rate near the discharge center for  $r \leq 2$  cm. For  $r > 2$  cm, ionization is not sufficient to sustain the electron transport, and therefore the anomalous factor increases to maintain the electron continuity.

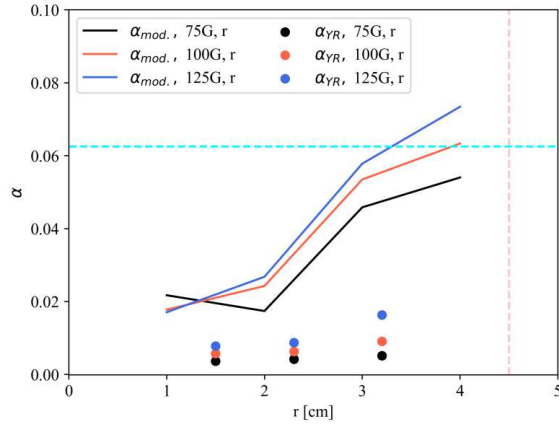


**Figure 10.** Anomalous parameter  $\alpha_{mod}$  as a function of radius, as determined by Eq. (13), for  $B = 75, 100$ , and  $125$  G. Also shown is the statistically determined anomalous parameter  $\alpha_{YR}$ . The cathode and anticathode radius  $R_{c,plate} = R_{atc} = 4.5$  cm is indicated by the vertical dashed line, and the value of the anomalous parameter determined by Bohm is indicated by the horizontal dashed line ( $\alpha = 1/16$ , Ref. <sup>40</sup>).

To explain the radial dependence of the anomalous transport, the radial dependence of the electron current terms from Eq. (7) are shown in Figure 11 in the case  $B = 100$  G. For  $r \geq 2$  cm the electron current due to ionization  $e\bar{R}_{iz}$  saturates. However, the absolute value of the gradient terms in the denominator of Eq. (7) continue to reduce for  $r \geq 2$  cm. The dominant term in the denominator is the electron pressure gradient  $\nabla p_e$ , which indeed shows a sharp decline in magnitude for  $r > 2$  cm (Appendix 2, Figure 21). Therefore, an enhancement in  $\alpha$  for  $r \geq 2$  cm occurs to compensate for the reduction in the electron pressure gradient, so that the radial electron current  $e\bar{\Gamma}_e^r$  can balance the injected beam current  $e\bar{\Gamma}_e^b$ .

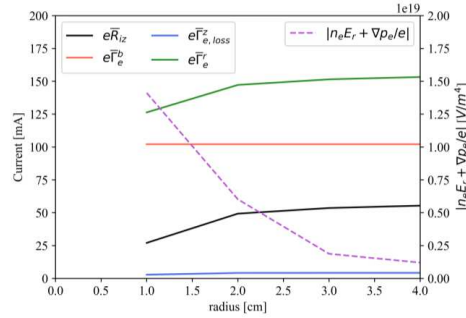


**Figure 11.** Radial dependence of electron current terms and denominator from Eq. (7), for the case  $B = 100$  G.

Using the experimentally determined radial profiles for the electron density, electron temperature, and ionization rate (Appendix 2), the radial ion current can be determined by solving Eqs. (8), (11), and (12) for  $e\bar{\Gamma}_i^r$ ,

$$e\bar{\Gamma}_i^r = 2\pi L_{ch} \int_0^r r' dr' R_{iz} - 2 \times 2\pi \int_0^r r' dr' (0.61 n_e v_{Bohm}). \quad (14)$$

Additionally, the radial outward ion velocity can be computed as

$$\bar{v}_{0i} = \bar{\Gamma}_i^r / 2\pi r L_{ch}. \quad (15)$$

The resulting values of  $e\bar{\Gamma}_i^r$  and  $\bar{v}_{0i}$  are shown in Figure 12. Evidently a radially outward ion current is necessary to satisfy global ion current continuity, generating an ion flow velocity that reaches approximately  $\bar{v}_{0i} = 350$  m/s in the radial outward direction. For  $r > 2$  cm, the radial ion current and resulting radial ion velocity reduce. This occurs since the volume integrated ionization rate saturates for  $r \geq 2$  cm (Appendix 2, Figure 19a), while the surface integrated Bohm ion current as determined by Eq. (12) leaving the cylindrical endcaps to either cathode and anticathode continues to increase linearly (Appendix 2, Figure 20). This steady state radial outflow of ions has been predicted in previous works of similar e-beam generated  $E \times B$  plasmas.<sup>41</sup> Doppler shift laser induced fluorescence (LIF) measurements are currently being conducted to directly measure the ion flow in the plasma and will be reported in a separate paper.<sup>42</sup>

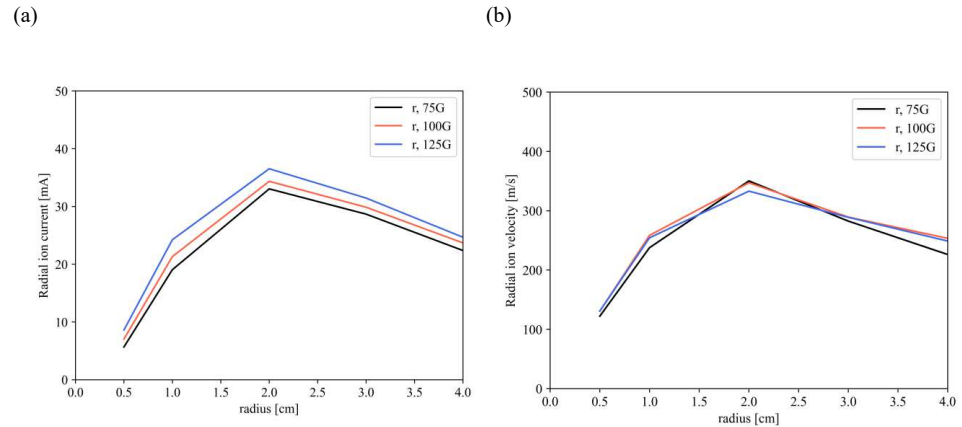


**Figure 12.** Radial dependence of (a) ion current  $e\bar{\Gamma}_i^r$  and (b) radial ion velocity determined by ion current continuity, for magnetic fields  $B = 75, 100, \text{ and } 125 \text{ G}$ .

## 2. Physical origins of multimodal azimuthal oscillations

The magnetic field scaling of the experimentally observed azimuthal modes are shown in Figure 13. Moreover, the  $f_0$  mode is amplified at larger radii  $r \geq 2 \text{ cm}$ , while the  $f_H$  mode decays at larger radii. The trend of increasing azimuthal modes frequency with increasing magnetic field is consistent with previous studies on similar  $E \times B$  devices.<sup>12,13,23</sup>

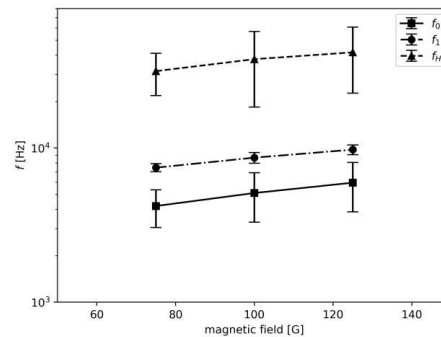


**Figure 13.** Frequency of  $f_0, f_1, \text{ and } f_H$  modes at radial position  $r = 3.2 \text{ cm}$ , as a function of applied magnetic field. Error bars in the mode frequency are given from the FWHM of the peaks in the cross-coherence spectrum. Experimental parameters are  $p = 0.1 \text{ mTorr}$ ,  $V_c = -55\text{V}$ .

The modified Simon-Hoh dispersion relation derived from the linearized fluid equations is given as<sup>43</sup>



$$\omega = \omega_{0i} + \frac{k^2 c_s^2}{2\omega_*} + \sqrt{\frac{k^4 c_s^4}{4\omega_*^2} + \frac{k^2 c_s^2}{\omega_*} (\omega_{0i} - \omega_0)}, \quad (16)$$

where  $k = (k_r^2 + k_\theta^2)^{1/2}$  is the wavevector amplitude,  $c_s = (k_B T_e / m_{Ar})^{0.5}$  is the bulk ion sound speed,  $\omega_{0i} = \mathbf{k} \cdot \mathbf{v}_{0i}$  is the ion response frequency corresponding to ion flow with velocity  $\mathbf{v}_{0i}$ ,  $\omega_0 = -k_\theta E_r / B$  is the electron  $\mathbf{E} \times \mathbf{B}$  frequency, and  $\omega_* = -k_\theta k_B T_e / e B L_n$  is the electron diamagnetic drift frequency with radial gradient length scale defined as  $L_n \equiv n_e (\partial n_e / \partial r)^{-1}$ . Instability occurs for  $\gamma \equiv \text{Im}(\omega) > 0$ . Importantly, electron  $\mathbf{E} \times \mathbf{B}$  flow is always destabilizing, while the ion response is destabilizing when there is ion flow counterpropagating with the wavevector, i.e.  $\mathbf{k} \cdot \mathbf{v}_{0i} < 0$ .

There are several mechanisms in which ion flow can contribute to the MSHI growth rate.<sup>13</sup> Here we consider the effect of the radially outward directed equilibrium ion flow velocity estimated from the ion continuity Eq. (15),  $\bar{v}_{0i} > 0$ . This ion flow is destabilizing for the case  $k_r < 0$ . Indeed, the PIC simulations indicate the existence of a spatially dependent wavevector  $\mathbf{k} = k_r \hat{\mathbf{r}} + k_\theta \hat{\boldsymbol{\theta}}$ , with  $k_r$  taking both positive and negative values (Figure 8). Therefore, these different processes associated with the ion flow may further destabilize the drift wave associated with Simon-Hoh Instability onset.

Using experimental radial profiles for the electron density (Figure 18a), electron temperature (Figure 18b), and plasma potential (Figure 19b), we determine radial profiles of  $\gamma$  for the cases with and without ion responses. Here we assume a single lobed ( $m = 1$ ) spoke centered at  $R_{c,plate}/2$ , such that the azimuthal wavenumber is  $k_\theta = 2/R_{c,plate}$ . Furthermore, in the cases where nonzero ion response is considered, the radial wavenumber is assumed to be single lobed in the radial direction, such that  $k_r = \pi/R_{c,plate}$ . However, as supported by the simulations (Figure 8), fine structures in the plasma density may form in the radial direction, indicating that the radial wavenumber may be significantly larger than considered here.

The calculated MSHI growth rate  $\gamma$  radial profiles are shown in Figure 14, considering the cases of no ion response and bulk ion velocity outward  $\bar{v}_{0i}$  as calculated by Eq. (15). Evidently,  $\gamma$  shows good agreement with the  $f_0$  and  $f_1$  modes under assumption of no ion response and outward ion flow respectively.

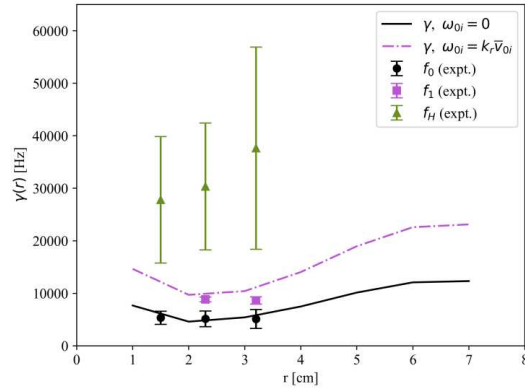


**Figure 14.** MSHI growth rate assuming  $\omega_{0i} = 0$ ,  $\omega_{0i} = k_r v_{0i}$ . Also shown are the experimentally determined  $f_0$ ,  $f_1$ , and  $f_H$  mode dependence on radius as determined by the azimuthal ion probe array. Experimental parameters are,  $B = 100$  G,  $p = 0.1$  mTorr,  $V_c = -55$  V.

This suggests future experimental studies and simulations should be carried out to precisely determine the ion dynamics and their role in the spoke formation in e-beam generated  $E \times B$  plasmas, for instance, using Doppler shift LIF.<sup>44,45</sup> MSHI theory as described by Eq. (16) does not predict the formation of harmonics or multiple simultaneous modes. We would also like to emphasize that the MSHI dispersion relation is based on linear theory and may not capture the full set of nonlinear or nonlocal physical mechanisms occurring in the saturated state of the spoke.<sup>19,43,46</sup> Furthermore, while this work has focused on oscillations in the  $r - \theta$  plane, the e-beam generated  $E \times B$  plasma considered here is inherently three-dimensional. Axial variations in plasma density and electric field may influence the azimuthal mode formation. Indeed, recent simulations have demonstrated the formation of helical structures in e-beam generated  $E \times B$  plasmas.<sup>47</sup>

## VI. Conclusion

In this work, we investigated the radial dependence of azimuthally propagating plasma oscillations in an electron beam generated  $E \times B$  plasma operated with an electron repelling anticathode. Experimental ion probe and fast frame imaging measurements indicate that at least 3 distinct azimuthal modes (with oscillation frequencies  $f_0$ ,  $f_1$ , and  $f_H$ ) simultaneously occur in the 5-50 kHz frequency band. Furthermore, the  $f_0$  and  $f_H$  modes exhibit a single-lobed ( $m = 1$ ) azimuthal mode number. These modes exhibit a complex radial dependence, with the lower frequency ( $f_0$ ) mode dominant near the plasma center and the higher frequency ( $f_H$ ) mode dominant in the peripheral plasma.

The experimental measurements are corroborated with a 2D3V PIC simulation, which is experimentally validated in this work and shows good agreement with time averaged radial

plasma density, electron temperature, and plasma potential profiles. The azimuthal mode spectrum observed in the PIC simulation corroborates the azimuthal mode spectrum determined experimentally with the ion probe array.

The radial dependence of the anticathode bias on the azimuthal oscillations is analyzed using a 1D electron continuity model. The model indicates that there is enhanced anomalous transport in the peripheral plasma region, which coincides with the growth of the additional azimuthal modes in this region. Furthermore, it is suggested that the suppression of anomalous transport in the central plasma region is caused by a balance of fluxes driven by ionization and electron pressure.

The physical mechanisms leading to the azimuthal mode spectrum are further analyzed by applying the linear theory of MSHI, making consideration of some possible mechanisms by which ion dynamics can affect the instability onset. We find that the lowest frequency ( $f_0$ )  $m = 1$  azimuthal mode is closely predicted by the MSHI dispersion relation by neglecting ion dynamics. By considering the radial outflow of ions calculated from solving the ion continuity, we find that the harmonic ( $f_1$ ) mode may be predicted by MSHI with reasonable agreement. However, the finding of multiple simultaneously occurring azimuthal modes is not predicted by MSHI with a simple equilibrium ion flow. Furthermore, even with the effect of radial ion flow taken into account, MSHI significantly underpredicts the higher frequency ( $f_H$ ) mode. Future studies should be conducted to investigate the relationship of azimuthal mode formation and resulting ion kinetics, potentially allowing development of e-beam  $E \times B$  plasmas with low ion energies in the peripheral plasma region that are more suited for material processing applications.

### Acknowledgements

This research was supported by the U.S. Department of Energy, Office of Fusion Energy Science, under Contract No. DEAC02-09CH11466, as a part of the Princeton Collaborative Low Temperature Plasma Research Facility (PCRF). The authors are grateful to Ivan Romadanov and Sunghyun Son for fruitful discussions regarding the physics of electron beam generated  $E \times B$  plasmas and cross field transport and Timothy K. Bennett for technical support on the electron beam chamber.

### Data Availability

The data that support the findings of this study are available from the corresponding author upon reasonable request.

## Appendix

### 1. Fast frame imaging corroboration of azimuthal plasma oscillations

An example fast frame image sequence of the optical plasma emission in the  $r - z$  plane of the plasma is shown in Figure 15.

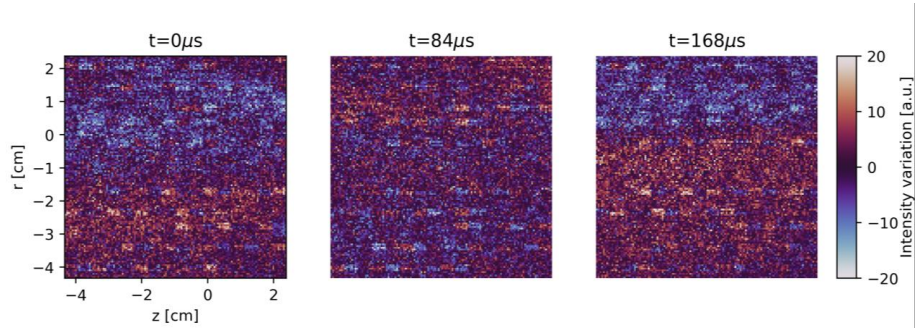


**Figure 15.** Mean subtracted fast frame image sequence of one cycle of the 6 kHz mode. Images are in the  $r - z$  plane, with radial coordinate on the vertical axis and axial coordinate on the horizontal axis. The red region indicates an optically brighter region of the plasma, while the blue region indicates optically dimmer, as compared to the time averaged brightness of the fast frame sequence. Experimental parameters are  $B = 100$  G,  $V_c = -55$  V.

The fast frame image sequences were collected for varying magnetic field  $B = 75, 100$ , and  $125$  G. Each frame was axially averaged, which yielded an optical intensity temporal signal  $\tilde{I}(r, t)$  for each radial position  $r$ . Spectrograms consisting of the Fourier transform of  $\tilde{I}(r, t)$  at each  $r$ ,  $F(\tilde{I})(r, f)$ , are shown in Figure 16. The fast frame spectrograms corroborate the azimuthal probe array measurements, indicating both the presence of  $f_0$  and  $f_H$  as azimuthally propagating modes.

This is the author's peer reviewed, accepted manuscript. However, the online version of record will be different from this version once it has been copyedited and typeset.

PLEASE CITE THIS ARTICLE AS DOI: 10.1063/5.0273397

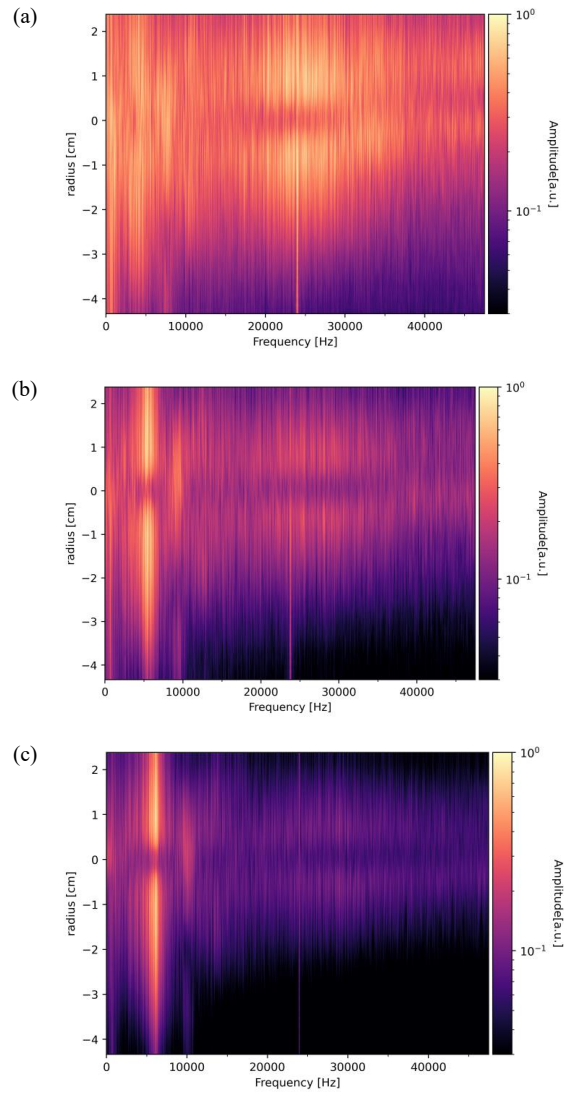


**Figure 16.** Spectrograms of the axially averaged fast frame sequence taken at 95 kfps for magnetic field (a)  $B = 75$  G, (b)  $B = 100$  G, and (c)  $B = 125$  G. Experimental parameters are  $p = 0.1$  mTorr,  $V_c = -55$  V.

## 2. Electron energy distribution function and macroscopic plasma parameters

The EEDFs and macroscopic parameters determined by Langmuir and emissive probes used in this work are shown in Figure 17, Figure 18, and Figure 19.

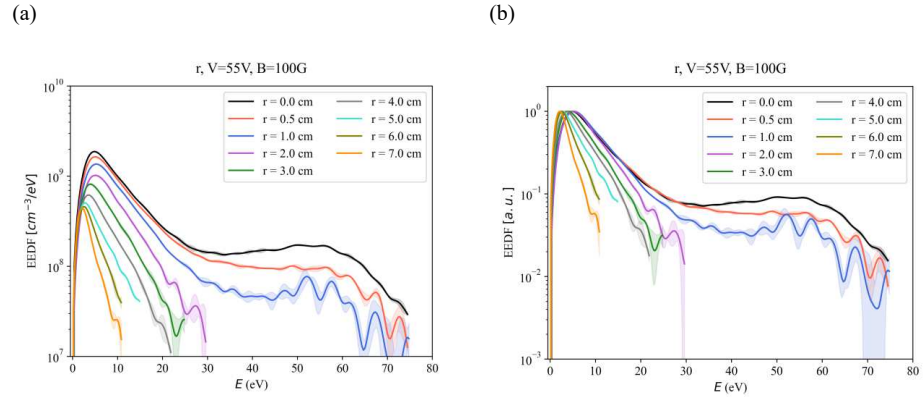


**Figure 17.** EEDF determined by LP at  $B = 100$  G,  $V_c = -55$  V,  $p = 0.1$  mTorr, for (a) in absolute units, (b) normalized to EEDF maximum.

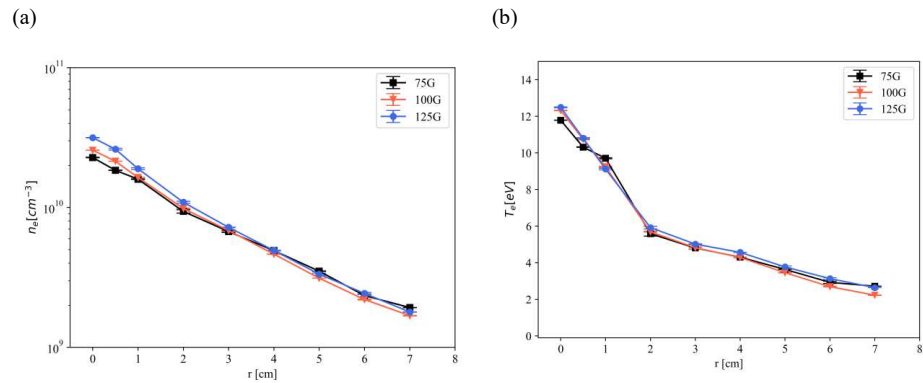


**Figure 18.** Radial profile of (a) plasma density  $n_e$  determined by LP and (b) electron temperature  $T_e$  for varying magnetic field,  $V_c = -55$  V,  $p = 0.1$  mTorr.

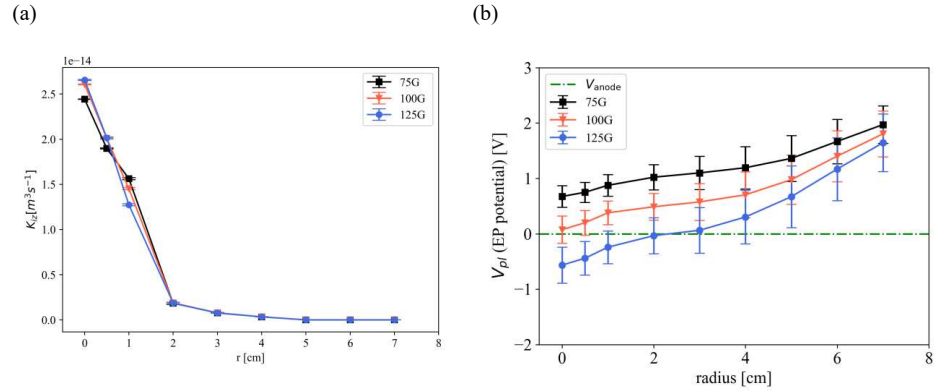


**Figure 19.** (a) Ionization rate constant  $K_{iz}$  radial profile determined by LP and (b) plasma potential  $V_{pl}$  radial profile determined by EP for varying magnetic field,  $V_c = -55$  V,  $p = 0.1$  mTorr.

The surface integrated Bohm ion current leaving the cylindrical endcaps to either cathode as determined by Eq. (12) is shown in Figure 20.

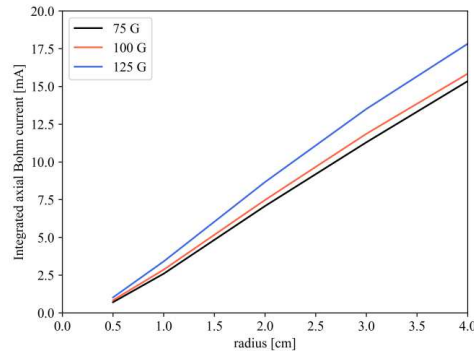


**Figure 20.** Surface integrated Bohm ion current as determined by Eq. (14), for varying magnetic field and parameters  $V_c = -55$  V,  $p = 0.1$  mTorr.

The radial profiles of electron pressure gradient inverse length scale and radial electric field as determined by LP and EP in this work are shown in Figure 21.

This is the author's peer reviewed, accepted manuscript. However, the online version of record will be different from this version once it has been copyedited and typeset.

PLEASE CITE THIS ARTICLE AS DOI: 10.1063/5.0273397

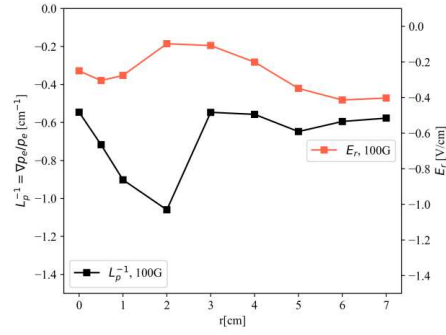


**Figure 21.** Radial profiles of electron pressure gradient inverse length scale  $L_p^{-1}$  and radial electric field for  $B = 100$  G,  $V_c = -55$  V,  $p = 0.1$  mTorr.



## References

- <sup>1</sup> F. Zhao, Y. Raitses, X. Yang, A. Tan, and C.G. Tully, "High hydrogen coverage on graphene via low temperature plasma with applied magnetic field," *Carbon* **177**, 244–251 (2021).
- <sup>2</sup> S.G. Walton, D.R. Boris, S.C. Hernández, E.H. Lock, Tz.B. Petrova, G.M. Petrov, and R.F. Fernsler, "Electron Beam Generated Plasmas for Ultra Low T<sub>e</sub> Processing," *ECS J. Solid State Sci. Technol.* **4**(6), N5033–N5040 (2015).
- <sup>3</sup> D.B. Zolotukhin, V.A. Burdovitsin, and E.M. Oks, "On the role of secondary electrons in beam plasma generation inside a dielectric flask by fore-vacuum plasma-cathode electron source," *Physics of Plasmas* **24**(9), 093502 (2017).
- <sup>4</sup> K.D. Schatz, and D.N. Ruzic, "An electron-beam plasma source and geometry for plasma processing," *Plasma Sources Sci. Technol.* **2**(2), 100–105 (1993).
- <sup>5</sup> S. Rauf, A. Balakrishna, A. Agarwal, L. Dorf, K. Collins, D.R. Boris, and S.G. Walton, "Three-dimensional model of electron beam generated plasma," *Plasma Sources Sci. Technol.* **26**(6), 065006 (2017).
- <sup>6</sup> S. Rauf, D. Sydorenko, S. Jubin, W. Villafana, S. Ethier, A. Khrabrov, and I. Kaganovich, "Particle-in-cell modeling of electron beam generated plasma," *Plasma Sources Sci. Technol.* **32**(5), 055009 (2023).
- <sup>7</sup> D.R. Boris, G.M. Petrov, E.H. Lock, T.B. Petrova, R.F. Fernsler, and S.G. Walton, "Controlling the electron energy distribution function of electron beam generated plasmas with molecular gas concentration: I. Experimental results," *Plasma Sources Sci. Technol.* **22**(6), 065004 (2013).
- <sup>8</sup> R.F. Fernsler, W.M. Manheimer, R.A. Meger, J. Mathew, D.P. Murphy, R.E. Pechacek, and J.A. Gregor, "Production of large-area plasmas by electron beams," *Physics of Plasmas* **5**(5), 2137–2143 (1998).
- <sup>9</sup> W.M. Manheimer, R.F. Fernsler, M. Lampe, and R.A. Meger, "Theoretical overview of the large-area plasma processing system (LAPPS)," *Plasma Sources Sci. Technol.* **9**, 370–386 (2000).
- <sup>10</sup> S. Yatom, N. Chopra, S. Kondeti, T.B. Petrova, Y. Raitses, D.R. Boris, M.J. Johnson, and S.G. Walton, "Measurement and reduction of Ar metastable densities by nitrogen admixing in electron beam-generated plasmas," *Plasma Sources Sci. Technol.* **32**(11), 115005 (2023).
- <sup>11</sup> L. Dorf, J.-C. Wang, S. Rauf, Y. Zhang, A. Agarwal, J. Kenney, K. Ramaswamy, and K. Collins, "Atomic precision etch using a low-electron temperature plasma," in *Atomic Precision Etch Using a Low-Electron Temperature Plasma*, edited by Q. Lin and S.U. Engelmann, (San Jose, California, United States, 2016), p. 97820J.
- <sup>12</sup> E. Rodríguez, V. Skoutnev, Y. Raitses, A. Powis, I. Kaganovich, and A. Smolyakov, "Boundary-induced effect on the spoke-like activity in  $E \times B$  plasma," *Physics of Plasmas* **26**(5), 053503 (2019).
- <sup>13</sup> Y. Sakawa, C. Joshi, P.K. Kaw, F.F. Chen, and V.K. Jain, "Excitation of the modified Simon–Hoh instability in an electron beam produced plasma," *Physics of Fluids B: Plasma Physics* **5**(6), 1681–1694 (1993).
- <sup>14</sup> M. Farley, P. Rose, and G. Ryding, "Freeman and Bernas Ion Sources," in *The Physics and Technology of Ion Sources*, edited by I.G. Brown, (Wiley-VCH Verlag GmbH & Co. KGaA, Weinheim, FRG, 2005), pp. 133–161.
- <sup>15</sup> F.F. Chen, "Radial Electric Field in a Reflex Discharge," *Phys. Rev. Lett.* **8**(6), 234–237 (1962).
- <sup>16</sup> J.P. Boeuf, and M. Takahashi, "New insights into the physics of rotating spokes in partially magnetized  $E \times B$  plasmas," *Physics of Plasmas* **27**(8), 083520 (2020).

- <sup>17</sup> J.W. Koo, and I.D. Boyd, "Modeling of anomalous electron mobility in Hall thrusters," *Physics of Plasmas* **13**(3), 033501 (2006).
- <sup>18</sup> M. Lee, K.-J. Chung, K. Hara, and J.Y. Kim, "Discharge mode transition in partially magnetized  $E \times B$  Penning discharge," *Physics of Plasmas* **31**(12), 123508 (2024).
- <sup>19</sup> O. Koshkarov, A. Smolyakov, Y. Raitses, and I. Kaganovich, "Self-Organization, Structures, and Anomalous Transport in Turbulent Partially Magnetized Plasmas with Crossed Electric and Magnetic Fields," *Phys. Rev. Lett.* **122**(18), 185001 (2019).
- <sup>20</sup> K. Hara, A.R. Mansour, and S. Tsikata, "Theory of gradient drift instabilities in low-temperature, partially magnetised plasmas," *J. Plasma Phys.* **88**(4), 905880408 (2022).
- <sup>21</sup> Y.-Q. Tao, R.W. Conn, L. Schmitz, and G. Tynan, "Collisionless Simon-Hoh instability in a strongly double-sheared electric field," *Physics of Plasmas* **1**(10), 3193–3198 (1994).
- <sup>22</sup> A. Likhanskii, A. Smolyakov, M. Papahn Zadeh, N. Chopra, and Y. Raitses, "3D effects in the simulations of the magnetized DC plasma sources for ion implantation, abstract ER2.00004," in *APS Gaseous Electronics Conference*, (2023).
- <sup>23</sup> M. Tyushev, M. Papahn Zadeh, V. Sharma, M. Sengupta, Y. Raitses, J.-P. Boeuf, and A. Smolyakov, "Azimuthal structures and turbulent transport in Penning discharge," *Physics of Plasmas* **30**(3), 033506 (2023).
- <sup>24</sup> N.S. Chopra, I. Romadanov, and Y. Raitses, "Anticathode effect on electron kinetics in electron beam generated  $E \times B$  plasma," *Plasma Sources Sci. Technol.* **33**(12), 125003 (2024).
- <sup>25</sup> Y. Raitses, D. Staack, A. Smirnov, and N.J. Fisch, "Space charge saturated sheath regime and electron temperature saturation in Hall thrusters," *Physics of Plasmas* **12**(7), 073507 (2005).
- <sup>26</sup> H.M. Mott-Smith, and I. Langmuir, "The Theory of Collectors in Gaseous Discharges," *Phys. Rev.* **28**(4), 727–763 (1926).
- <sup>27</sup> P. Welch, "The use of fast Fourier transform for the estimation of power spectra: A method based on time averaging over short, modified periodograms," *IEEE Trans. Audio Electroacoust.* **15**(2), 70–73 (1967).
- <sup>28</sup> L.B. White, and B. Boashash, "Cross spectral analysis of nonstationary processes," *IEEE Trans. Inform. Theory* **36**(4), 830–835 (1990).
- <sup>29</sup> L. Fedeli, A. Huebl, F. Boillod-Cerneux, T. Clark, K. Gott, C. Hillairet, S. Jaure, A. Leblanc, R. Lehe, A. Myers, C. Piechurski, M. Sato, N. Zaim, W. Zhang, J.-L. Vay, and H. Vincenti, "Pushing the Frontier in the Design of Laser-Based Electron Accelerators with Groundbreaking Mesh-Refined Particle-In-Cell Simulations on Exascale-Class Supercomputers," in *SC22: International Conference for High Performance Computing, Networking, Storage and Analysis*, (IEEE, Dallas, TX, USA, 2022), pp. 1–12.
- <sup>30</sup> M. Tyushev, M. Papahn Zadeh, N.S. Chopra, Y. Raitses, I. Romadanov, A. Likhanskii, G. Fubiani, L. Garrigues, R. Groenewald, and A. Smolyakov, "Mode transitions and spoke structures in  $E \times B$  Penning discharge," *Physics of Plasmas* **32**(1), 013511 (2025).
- <sup>31</sup> L.C. Pitchford, L.L. Alves, K. Bartschat, S.F. Biagi, M.C. Bordage, A.V. Phelps, C.M. Ferreira, G.J.M. Hagelaar, W.L. Morgan, S. Pancheshnyi, V. Puech, A. Stauffer, and O. Zatsarinny, "Comparisons of sets of electron-neutral scattering cross sections and swarm parameters in noble gases: I. Argon," *J. Phys. D: Appl. Phys.* **46**(33), 334001 (2013).
- <sup>32</sup> C. Yamabe, S.J. Buckman, and A.V. Phelps, "Measurement of free-free emission from low-energy-electron collisions with Ar," *Phys. Rev. A* **27**(3), 1345–1352 (1983).
- <sup>33</sup> O. Zatsarinny, and K. Bartschat, " $B$ -spline Breit-Pauli  $R$ -matrix calculations for electron collisions with argon atoms," *J. Phys. B: At. Mol. Opt. Phys.* **37**(23), 4693–4706 (2004).

- <sup>34</sup> L. Xu, D. Eremin, and R.P. Brinkmann, "Direct evidence of gradient drift instability being the origin of a rotating spoke in a crossed field plasma," *Plasma Sources Sci. Technol.* **30**(7), 075013 (2021).
- <sup>35</sup> A. Simon, "Ambipolar Diffusion in a Magnetic Field," *Phys. Rev.* **98**(2), 317–318 (1955).
- <sup>36</sup> D. Curreli, and F.F. Chen, "Cross-field diffusion in low-temperature plasma discharges of finite length," *Plasma Sources Sci. Technol.* **23**(6), 064001 (2014).
- <sup>37</sup> S. Yoshikawa, and D.J. Rose, "Anomalous Diffusion of a Plasma across a Magnetic Field," *The Physics of Fluids* **5**(3), 334–340 (1962).
- <sup>38</sup> J.P. Boeuf, and L. Garrigues, "Low frequency oscillations in a stationary plasma thruster," *Journal of Applied Physics* **84**(7), 3541–3554 (1998).
- <sup>39</sup> J. Bareilles, G.J.M. Hagelaar, L. Garrigues, C. Boniface, J.P. Boeuf, and N. Gascon, "Critical assessment of a two-dimensional hybrid Hall thruster model: Comparisons with experiments," *Physics of Plasmas* **11**(6), 3035–3046 (2004).
- <sup>40</sup> D. Bohm, E.H.S. Burhop, and H.S.W. Massey, *The Characteristics of Electrical Discharges in Magnetic Fields* (McGraw-Hill, 1949).
- <sup>41</sup> N.S. Chopra, I. Romadanov, and Y. Raites, "Production of warm ions in electron beam generated E x B plasma," *Applied Physics Letters* **124**(064101), (2024).
- <sup>42</sup> S. Son, I. Romadanov, N. Chopra, and Y. Raites, "GP12.026: Measurements of two-dimensional ion velocity distributions in electron beam generated E x B plasma," (APS Division of Plasma Physics, Atlanta, GA, 2024).
- <sup>43</sup> A.I. Smolyakov, O. Chapurin, W. Frias, O. Koshkarov, I. Romadanov, T. Tang, M. Umansky, Y. Raites, I.D. Kaganovich, and V.P. Lakhin, "Fluid theory and simulations of instabilities, turbulent transport and coherent structures in partially-magnetized plasmas of ExB discharges," *Plasma Phys. Control. Fusion* **59**(1), 014041 (2017).
- <sup>44</sup> A.M. Keesee, E.E. Scime, and R.F. Boivin, "Laser-induced fluorescence measurements of three plasma species with a tunable diode laser," *Review of Scientific Instruments* **75**(10), 4091–4093 (2004).
- <sup>45</sup> I. Romadanov, and Y. Raites, "A confocal laser-induced fluorescence diagnostic with an annular laser beam," *Review of Scientific Instruments* **94**(7), 073002 (2023).
- <sup>46</sup> I. Romadanov, A. Smolyakov, Y. Raites, I. Kaganovich, T. Tian, and S. Ryzhkov, "Structure of nonlocal gradient-drift instabilities in Hall E x B discharges," *Physics of Plasmas* **23**(12), 122111 (2016).
- <sup>47</sup> J. Chen, A.T. Powis, I.D. Kaganovich, and Z. Wang, "Three-dimensional Helical-rotating Plasma Structures in Beam-generated Partially Magnetized ExB Plasmas," arXiv:2501.01161 [Physics.Plasma-Ph], (2025).